

submitted to **Journal of Space Weather and Space Climate**  
 © The author(s) under the Creative Commons Attribution-NonCommercial license

# Improvements on coronal hole detection in SDO/AIA images using supervised classification

Martin A. Reiss<sup>1</sup>, Stefan J. Hofmeister<sup>1</sup>, Ruben De Visscher<sup>2</sup>, Manuela Temmer<sup>1</sup>,  
 Astrid M. Veronig<sup>1</sup>, Véronique Delouille<sup>2</sup>, Benjamin Mampaey<sup>2</sup>, Helmut  
 Ahammer<sup>3</sup>

<sup>1</sup> University of Graz, IGAM-Kanzelhöhe Observatory, NAWI Graz, Graz, Austria

e-mail: [martin.reiss@uni-graz.at](mailto:martin.reiss@uni-graz.at)

<sup>2</sup> Royal Observatory of Belgium, Brussels, Belgium

e-mail: [veronique.delouille@oma.be](mailto:veronique.delouille@oma.be)

<sup>3</sup> Medical University of Graz, Institute of Biophysics, Graz, Austria

Received 19 December 2014 / Accepted 20 June 2015

## ABSTRACT

We demonstrate the use of machine learning algorithms in combination with segmentation techniques in order to distinguish coronal holes and filaments in SDO/AIA EUV images of the Sun. Based on two coronal hole detection techniques (intensity-based thresholding, SPoCA), we prepared data sets of manually labeled coronal hole and filament channel regions present on the Sun during the time range 2011 - 2013. By mapping the extracted regions from EUV observations onto HMI line-of-sight magnetograms we also include their magnetic characteristics. We computed shape measures from the segmented binary maps as well as first order and second order texture statistics from the segmented regions in the EUV images and magnetograms. These attributes were used for data mining investigations to identify the most performant rule to differentiate between coronal holes and filament channels. We applied several classifiers, namely Support Vector Machine, Linear Support Vector Machine, Decision Tree, and Random Forest and found that all classification rules achieve good results in general, with linear SVM providing the best performances (with a true skill statistic of  $\approx 0.90$ ). Additional information from magnetic field data systematically improves the performance across all four classifiers for the SPoCA detection. Since the calculation is inexpensive in computing time, this approach is well suited for applications on real-time data. This study demonstrates how a machine learning approach may help improve upon an unsupervised feature extraction method.

**Key words.** Solar wind – Coronal holes – Filament channels – Feature extraction – Supervised Classification – Textural features

## 1. Introduction

Coronal holes play an important role in geomagnetic storm activity (Tsurutani et al., 2006) and are the dominant contributors to space weather disturbances at times of quiet solar activity. The term

coronal hole is commonly associated with regions of one dominant magnetic polarity with rapidly expanding open magnetic field lines along which solar wind particles escape into interplanetary space (Gosling and Pizzo, 1999; Cranmer, 2009). Coronal holes are the source regions of the high speed solar wind streams (HSSs). In combination with the Sun's rotation, they shape the solar wind distribution in interplanetary space. In Extreme Ultraviolet (EUV) and X-ray images of the Sun, coronal holes are visible as dark areas in the solar corona due to their lower temperature and electron density compared to the ambient coronal plasma (Munro and Withbroe, 1972).

The detection of coronal holes purely from their low intensity in solar EUV images is a challenging task since filament channels also appear as dark coronal features. Filament channels are usually interpreted in terms of the weakly twisted flux rope model, having a magnetic field which is dominated by the axial component. Dense prominence material is located in the dip of the helical windings leading to the elongated dark structures observed at a similar dark intensity level as coronal holes (Mackay et al., 2010; de Toma, 2011).

In the past, coronal holes have mostly been identified and tracked by experienced observers. There have been recent attempts to automate the process for the identification and detection of coronal holes (Barra et al., 2007; Kirk et al., 2009; Krista and Gallagher, 2009; Rotter et al., 2012). Those detection techniques are mainly based on differences in intensity compared to the ambient corona.

The extraction of coronal holes is of interest for various applications in astrophysics, e.g. the forecast of HSSs. The areas of coronal holes extracted at the solar meridian reveal a correlation with the solar wind speed measured  $\sim$ 4 days later in-situ at 1 AU (Vršnak et al., 2007; Verbanac et al., 2011; Rotter et al., 2012; Rotter et al., 2015). This relation enables us to forecast HSSs based on coronal hole observations. Thus, it is important to improve the coronal hole detection method, in order to exclude filaments that may erroneously be identified as a coronal hole region in EUV images.

In this work, Solar Dynamic Observatory (SDO) Atmospheric Imaging Assembly (AIA) 19.3 nm images (Lemen et al., 2012) and SDO/ Helioseismic and Magnetic Imager (HMI) magnetograms (Scherrer et al., 2012) are used in order to analyse the properties of coronal holes and filament channels during the period 2011 January 1 till 2013 December 31. We first obtain low intensity regions from SDO/AIA 19.3 nm images by means of two coronal hole detection techniques: one using intensity thresholding (Rotter et al., 2012), and a second, called SPoCA (Verbeeck et al., 2014), based on fuzzy clustering of intensity values. Comparing these detections with H $\alpha$  filtergrams from Kanzelhöhe Observatory (Austria) in which filaments can be clearly identified (Pötzi et al., 2015), we label these regions as either 'filament' or 'coronal hole'. The detected regions were mapped onto the corresponding HMI line-of-sight magnetograms. This allows us to calculate a set of attributes that takes into account EUV intensity and binary shape information as well as the magnetic field structure for each of the regions.

Our contribution in this paper is two-fold. First, we devise decisive coronal feature attributes. We focus on the magnetic flux imbalance, first and second order image statistics and shape measures since: (i) coronal holes are expected to be characteristic regions of one dominant magnetic polarity whereas filament channels are regions of closed magnetic field lines along a magnetic field reversal line; (ii) the physical properties of filament channels are partly reflected in their geometric characteristics. Filament channels are, in contrast to coronal holes, in most cases observable as elongated structures that extend in a particular direction.

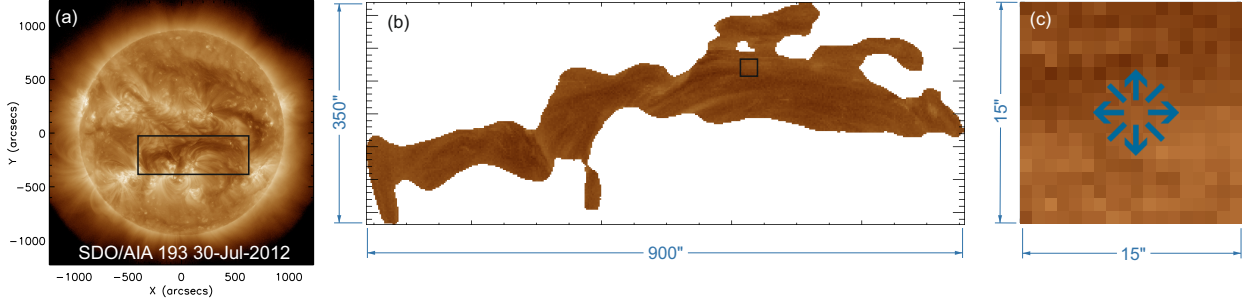


**Fig. 1.** Analysis of the detected low intensity regions. (a) AIA 19.3 nm image from 30-Jul-2012 showing a filament channel; (b) Detected filament channel from EUV image based on intensity thresholding; (c) Illustration of the spatial relationship of pixel values contained in the filament channel.

Second, we insert the computed attributes into various supervised classification schemes in order to design the most suitable decision rule for a differentiation in real-time. We tested and compared through cross-validation four commonly used classifiers, namely Support Vector Machine (SVM), Linear SVM, Decision Tree, and Random Forest. To evaluate the performance of different classifiers we made use of the Hanssen & Kuipers discriminant, also known as true skill statistics (TSS) (Hanssen and Kuipers, 1965; Bloomfield et al., 2012), as a quantitative measure. This paper is structured in the following way: In Section 2 the preparation of the labeled data sets is explained. A description of the proposed attributes is given in Section 3 and the applied supervised classification schemes are presented in Section 4. The results are given in Section 5 and their implications are discussed in Section 6.

## 2. Data preparation

Two different coronal hole segmentation techniques (intensity-based thresholding (Rotter et al., 2012; Rotter et al., 2015), SPoCA (Verbeeck et al., 2014)) were applied in order to prepare two data sets of low intensity regions during the period 2011 January 1 till 2013 December 31. Based on these data we created training sets to design the most suitable decision rule for a differentiation of coronal hole and filament channel regions.

### 2.1. Coronal hole feature extraction

#### 2.1.1. Intensity-based thresholding

An intensity-based thresholding technique was used to detect low intensity regions in SDO/AIA 19.3 nm images. Based on the intensity distribution in the full-disk EUV images we apply a threshold value of  $0.38 \times (\text{median intensity value})$  for areas within  $\pm 60^\circ$  longitude and latitude. Due to the optically thin emission from neighboring coronal structures, we used an additional multiplication factor of 1.6 for areas outside the  $\pm 60^\circ$  longitude and latitude window. With this refinement, polar coronal holes are also well detected although they have a smaller contrast. From this we created binary maps, which were post-processed by using morphological methods (erosion, dilation). The

effects of these operators on binary maps are to erode (or shrink) the boundaries of regions, removing all small anomalies (erosion) and to gradually expand the boundaries of regions to fill small holes in-between (dilation). A  $16 \times 16$  pixel kernel was used to remove small artefacts and fill small gaps in the extracted regions.

### 2.1.2. Fuzzy clustering

The SPoCA-suite ([Verbeeck et al., 2014](#)) is a set of segmentation procedures that allows decomposition of an EUV image into regions of similar intensity, typically active regions, coronal holes, and quiet sun. In the framework of the Feature Finding Team project (FFT; [Martens et al. \(2012\)](#)), the SDO Event Detection System (SDO EDS; [Hurlbut et al. \(2012\)](#)) runs the SPoCA-suite to extract coronal hole information from AIA images in the 19.3 nm passband, and upload the entries every four hours to the Heliophysics Events Knowledgebase ([Hurlbut et al., 2012](#)). These entries are searchable through the graphical interface iSolSearch, the ontology software package of IDL Solarsoft, and the JHelioviewer visualization tool ([Müller et al., 2009](#)).

The SPoCA extraction method for coronal holes relies on the Fuzzy C-Means algorithm (FCM) ([Bezdek, 1981](#)). It clusters the pixel's intensity values into four classes through the minimization of the intra-cluster variance. Such minimization leads to an iterative algorithm, where at each iteration every pixel is assigned a membership value between 0 and 1 to each one of the class, then the class centers are computed using these memberships. These steps are repeated until convergence of the class centers. The segmented map is obtained by attributing a pixel to the class for which it has the maximum final membership value. The coronal hole map corresponds to the class whose center has the lowest intensity value. Various preprocessing steps are performed before applying FCM algorithm: Images are calibrated using the IDL Solarsoft `aia_prep` routine, and intensities are normalized by their median values. We correct for the limb brightening effect by fitting a smooth transition function and inverting it. Finally, a square-root transform is applied on the images. Indeed, [Anscombe \(1948\)](#) showed that for Poisson distributed data a square-root transform induces exact asymptotic normality and stabilizes the variance. This is especially useful for the extraction of low-intensity regions which are affected by Poisson noise.

Once the segmented maps are obtained, some post-processing is needed to extract individual low intensity regions. Elements with a radius smaller than 6 arcsec are removed and neighbouring connected components within a 64 arcsec distance are aggregated. Coronal holes candidates having an area smaller than  $3000 \text{ arcsec}^2$  are discarded. A study of low intensity feature detected by SPoCA during the month of January 2011 revealed that coronal hole candidates detected for more than three consecutive days exhibit the expected magnetic properties characteristic of unipolar regions, which was not the case for shorter lived regions. Setting up a threshold on lifetime is thus a valuable tool to eliminate spurious dark regions. Hence only low-intensity regions which live longer than three days are included in the final coronal hole maps used here and in the SDO EDS pipeline (we refer to [Verbeeck et al. \(2014\)](#) for more details).

## 2.2. Labeled datasets

The extracted regions were manually labeled as either ‘filament’ or ‘coronal hole’ regions by visually inspecting  $H\alpha$  filtergrams from Kanzelhöhe Observatory (Austria). We selected only regions greater than  $1900 \text{ arcsec}^2$  for which Kanzelhöhe  $H\alpha$  data were available and that were located close

to the central meridian ( $\pm 30^\circ$  in longitude/latitude). If at the position of an extracted low intensity region a filament was clearly observable in the corresponding H $\alpha$  filtergram (to take into account the evolution of filament material we checked a time span of three days), the structure was labeled as ‘filament’. Otherwise, the structure was labeled as ‘coronal hole’. This procedure was performed for both segmentation methods once per day, resulting in two training sets: one containing 349 coronal holes and 61 filaments for the intensity-based thresholding method and the second with 252 coronal holes and 46 filaments for the SpoCA algorithm. In addition we mapped the extracted regions onto HMI line-of-sight magnetograms to quantify the magnetic flux characteristics in the extracted regions. Note that both segmentation methods have different capabilities for extracting low-intensity regions, which explains the dissimilarity in the number of CH candidates detected. In future works, we plan on comparing more exhaustively these two methods.

### 3. Proposed attributes

On the prepared training datasets we investigate shape measures, magnetic flux properties and first and second order image statistics for the calculation of characteristic attributes. Shape measures were used to characterize the shape of the detected low intensity regions. The calculated shape measures also allow us to reduce the object pixel configuration contained in a binary map of a structure to a single scalar number. With the help of first order and second order image statistics (Haralick et al., 1973; Weyn et al., 2000; Ahammer et al., 2008) we focus on the overall pixel value distribution and the spatial relation between pixel values contained in AIA EUV images and HMI line-of-sight magnetograms. Second order statistics, originally applied on grey scale images, was adapted to open value ranges (i.e. including negative data values) in order to calculate textural features for intensity and magnetic field configurations. This enables us to characterize the intrinsic texture information contained in the extracted structures in AIA 19.3 nm and line-of-sight magnetograms via the computation of a set of textural features. A description of the proposed methods is outlined in the following subsections.

#### 3.1. Shape Measures

While many shape descriptors exist, there exists no generally accepted definition in literature. In order to investigate irregular shapes of coronal holes and filament channels in detail, two alternative shape measurements were developed.

**Symmetry analysis** Shapes are intuitively described with the terms symmetric or asymmetric. We measure geometrical symmetry properties with the following technique: After the application of discrete geometrical transformations like rotation, reflection and a composition of both, the relative overlap in percentage is calculated.

**Direction-dependent shape analysis** Shapes can also be presented in form of a function, e.g. the average number of neighbours in each direction is representative for the relevant shape information of an object. For a detailed description of the used shape measures we refer to Reiss et al. (2014).

### 3.2. Magnetic Flux Imbalance

We characterize the magnetic flux imbalance in the detected features by calculating the following two attributes from the line-of-sight magnetograms:

$$R_1 = \frac{n_+}{n_-}, \quad (1)$$

i.e. the ratio of the number of positive ( $n_+$ ) and negative ( $n_-$ ) pixel values, and

$$R_2 = 2 \left| \frac{1}{2} - \frac{\Phi_+}{\Phi_+ + |\Phi_-|} \right|, \quad (2)$$

with  $\Phi_+$  being the total positive magnetic flux in the segmented feature, and  $\Phi_-$  being the total negative flux.  $R_2$  quantifies the imbalance between the total positive and the total magnetic flux within the extracted regions. In the ideal case, this value would be 1 for coronal holes, as regions of a unique polarity ( $\Phi_+ = 0$  or  $\Phi_- = 0$ ), and 0 for filament channels ( $\Phi_+ = \Phi_-$ ), as magnetically bipolar regions orientated along a polarity inversion line.

### 3.3. First Order Image Statistics

Pixel values contained in the extracted regions were rounded to the nearest integer value. The probability  $P(i)$  for the occurrence of pixels with integer value  $i$  is defined as

$$P(i) = \frac{n(i)}{N}, \quad (3)$$

where  $n(i)$  is defined as the number of pixels with the actual pixel value  $i$  and  $N$  is the total number of image pixels. The following standard first order attributes were used:

$$\text{Mean: } \mu = \sum_i i P(i), \quad (4)$$

$$\text{Variance: } \sigma^2 = \sum_i (i - \mu)^2 P(i), \quad (5)$$

$$\text{Standard Deviation (Contrast): } C_1 = \sqrt{\sigma^2}, \quad (6)$$

$$\text{Energy: } E_1 = \sum_i P(i)^2, \quad (7)$$

$$\text{Entropy: } S_1 = \sum_i -P(i) \log(P(i)). \quad (8)$$

Variance  $\sigma^2$  and contrast  $C_1$  are associated with the width of the pixel value distribution. High variance or contrast indicate large pixel value differences. Energy  $E_1$  is high for unevenly distributed pixel values independent of the designated pixel value itself. High entropy  $S_1$  values reflect the degree of information content within the pixel value distribution. Low entropy values correspond to coherent pixel values with low information content. High values reflect highly disordered image values with a high amount of intrinsic information content.

### 3.4. Second Order Image Statistics

Second order statistics (Haralick et al., 1973; Weyn et al., 2000; Ahammar et al., 2008) are utilized for the calculation of textural features of AIA and HMI images providing information about the spatial arrangement of pixel values. A set of matrices  $n_{\phi,d}(i, j)$  count how many times a given combination of pixel values  $i$  and  $j$  occur in a particular spatial arrangement. The probabilities of co-occurrences of pixel values can then be represented with the so called co-occurrence matrix  $C(i, j)$ . The basic idea how spatial information is contained in low intensity regions is illustrated in Figure 1. Textural features allow the description of textural information with a set of scalar numbers.

#### 3.4.1. Co-Occurrence Matrix

Analogous to the probability  $P(i)$  for the occurrence of pixels with value  $i$ , we define  $P_{\phi,d}(i, j)$  indicating the probability for the co-occurrence of pixel value  $i$  and pixel value  $j$  in a given distance  $d$  and direction  $\phi$ .  $n_{\phi,d}(i, j)$  is the total number of co-occurrences of pixel value  $i$  with pixel value  $j$  within the distance  $d$  and direction  $\phi$ . The matrix  $P_{\phi,d}(i, j)$  is defined as

$$P_{\phi,d}(i, j) = \frac{n_{\phi,d}(i, j)}{N}, \quad (9)$$

where  $N$  is the total number of object pixels. Since there is no consensus about the choice of angles  $\phi$  and distance  $d$ , the calculations have been done with a distance of one pixel and 8 directions considering only the nearest neighbourhood of each pixel. The used set of angles  $\Omega = \{\phi_0, \dots, \phi_7\}$  is given by

$$\phi_l = l \cdot 45^\circ, \quad l = 0, \dots, 7, \quad \phi_l \in \Omega. \quad (10)$$

This set of angles provides 8 matrices  $P_{\phi,d}(i, j)$ , one matrix for each of the directions. The co-occurrence matrix  $C(i, j)$  is finally defined as

$$C(i, j) = \text{avg} (P_{\phi,d}(i, j)). \quad (11)$$

The entry  $(i, j)$  in the co-occurrence matrix  $C(i, j)$  therefore indicates the probability for the co-occurrence of pixel value  $i$  with pixel value  $j$  within the nearest neighbourhood. In Figure 2 the corresponding co-occurrence matrix for a filament channel, shown in Figure 1, is visualized. For the implementation it is necessary to differentiate between the actual pixel value and the position in the co-occurrence matrix.

Important properties of the co-occurrence matrix  $C(i, j)$  are represented in Figure 2: (i)  $C(i, j)$  is always a symmetric matrix since the number of occurrences for pixel value  $i$  together with pixel value  $j$  will be always the same as vice versa. (ii)  $C(i, j)$  provides a probability density function (PDF), to find probabilities of joint relationships between a pair of pixel values  $i$  and  $j$ . Thus, the sum over all entries must be equal to 1.

#### 3.4.2. Textural Features

A set of textural features (Appendix A) can be calculated from the co-occurrence matrix  $C(i, j)$ . For illustrative propose, we discuss two textural features (energy  $H_1$  and contrast  $H_2$ ) in detail:

$$H_1 = \sum_i \sum_j C(i, j)^2, \quad (12)$$

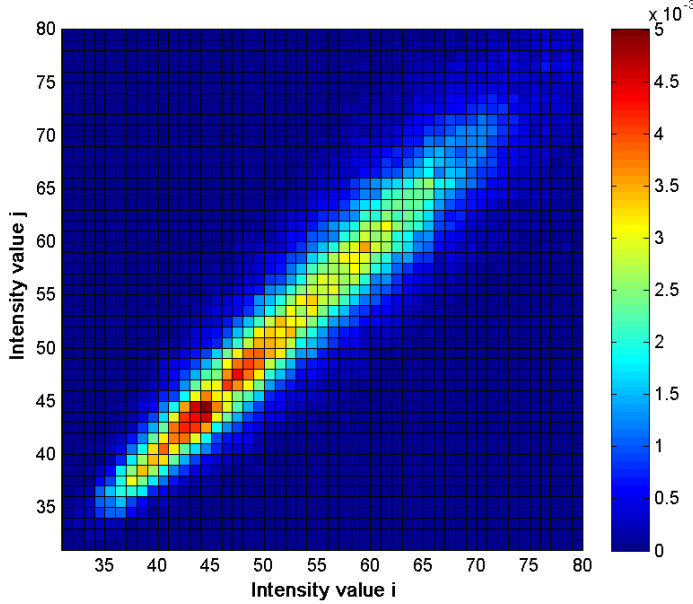


**Fig. 2.** Representation of the co-occurrence matrix  $C(i, j)$  calculated from the filament channel shown in Figure 1. The colorbar of the co-occurrence matrix entries  $C(i, j)$  represent the probability for neighbouring occurrences of pixel value  $i$  with pixel value  $j$ .

$$H_2 = \sum_i \sum_j (i - j)^2 C(i, j). \quad (13)$$

Energy  $H_1$  is a measure of homogeneity of the pixel pair distribution. It is high for a small number of different pixel pair combinations and low for a large number of different combinations.  $H_1$  is at its maximum if the image contains only a single pixel value, independent of the pixel value itself. Thus, the energy is mainly a measure of the sharpness of the peak in the co-occurrence matrix. It is high for a sharp peak, indicating only a few pixel value combinations, and low for a broad peak, indicating a variety of pixel value combinations.

Due to the quadratic influence of the differences in the contrast  $H_2$ , the value is high for large differences between pixel value  $i$  and pixel value  $j$ . Hence, mainly the position of the peak in the co-occurrence matrix is important (see Figure 2). The position indicates small or large differences of the pixel values. The contrast feature is a measure of the amount of local variations present in the image. It is high for large differences of pixel pair values and low for small differences. All textural features that were used in this analysis are listed in Appendix A.

## 4. Supervised classification problem

The computed attributes were used as input for data mining in order to design the most suitable decision rule for a separation between coronal holes and filaments. Supervised classification is commonly applied when a large set of attributes is available and the interpretation of the obtained information is complicated. In supervised classification problems, an object is observed and we

aim to classify it into one of two classes (0 or 1, here ‘filament’ or ‘coronal hole’). To make this decision we have access to measurements of various properties of the object, called *features*. Given these feature vectors  $\mathbf{x} \in R^d$ , we aim to find a decision (or classification) rule, that is, a mapping  $c : R^d \rightarrow \{0, 1\}$ , where  $c(\mathbf{x})$  indicates the decision when feature vector  $\mathbf{x}$  is observed. Out of the numerous collection of possible decision rules, we aim to identify those performing best. Four widely used algorithms with proven theoretical properties (Section 4.1) are evaluated via a common protocol (Section 4.2). Section 5 describes the performance measures used to compare them.

The set of attributes described in Section 3.1-3.4 together with the labelling of the maps as ‘filament’ or ‘coronal hole’ provide us with a labeled dataset of feature values. We consider two situations. First, the whole set of attributes, computed with both SDO/AIA and SDO/HMI from SPoCA, is used as feature values with the aim to reach the best classification. Second, we create new classifiers trained on a sub-set of attributes using only AIA information on SPoCA maps. The aim is twofold: (i) obtain a set of rules that are easy to implement into the SDO EDS pipeline, (ii) measure the corresponding improvement in performance for the SPoCA algorithm.

#### 4.1. Supervised classification algorithms

We tested four classifiers using the scikit-learn library (Pedregosa et al., 2011):

**Linear Support Vector Machine** The key idea of Linear Support Vector Machine (Linear SVM) is to find hyperplanes that separate the data as much as possible, that is, with a large margin. SVM optimizes a trade-off between maximizing the margin of separability between classes and minimizing margin errors. It provides a convex approximation to the combinatorial problem of minimizing classification errors. The practical implementation is formulated as the minimization of a penalized loss function. We used the LIBLINEAR (Fan et al., 2008) implementation of Linear SVM.

**Support Vector Machine** A second key idea of SVM as presented by Vapnick in his original formulation (Vapnick, 1998) is to map the feature vectors in a nonlinear way to a high (possibly infinite) dimensional space and then utilize linear classifiers in this new space. This is done through the use of a kernel function. In our case, we tried several kernel functions: gaussian, sigmoid, polynomial and linear from the LIBSVM library (Chang and Lin, 2011).

**Decision Tree** Decision trees produce a set of if-then-else decision rules that are selected on the basis of the expected reduction in entropy that would result from sorting a particular attribute. Trees are usually grown to their maximum size before a pruning step is applied to reduce over-fitting. Various decision tree algorithms have been proposed (Breiman et al., 1984; Quinlan, 1993). For this work we used decision trees using the Gini and entropy criteria and various depths and splitting rules<sup>1</sup>.

**Random Forest** We tested an ensemble classifier method<sup>2</sup>. More precisely, we used Random Forest, where a set of decision trees is created by introducing some randomness in the construction of the decision tree. The prediction of the ensemble is given as the averaged prediction of the individual decision tree (Breiman, 1998).

<sup>1</sup> <http://scikit-learn.org/stable/modules/tree.html>

<sup>2</sup> <http://scikit-learn.org/stable/modules/ensemble.html>

#### 4.2. Training and evaluation protocol

The supervised classification in machine learning is always performed in two steps. 1.) During the training phase, a model is estimated from the data. 2.) In the validation (or test-) phase the trained model is applied on other data and model properties (such as error classification rate) are estimated. This is done in practice by splitting the initial data set into a ‘training dataset’ and a ‘validation dataset’.

However, in the present study we want to compare the performance of several classifiers. In this case, performing the splitting only once is not enough, as the observed difference between two classifiers may depend on the chosen training and test samples. To avoid this, we need to repeat the comparison over randomly selected partitions of the data and report the average performance (see Chap. 5 in [Japkowics and Shah \(2014\)](#) for a discussion on error estimation in classification problem).

We therefore perform 100 iterations of the following protocol. We do a stratified shuffle-split of the original dataset into a 75% development set and 25% evaluation set. This means that we shuffle the original dataset, then split it into two 75% / 25% subsets (shuffle-split) where each subset has approximately the same class distributions as the full dataset (stratification). The development set in each iteration is used to train and evaluate each hyper-parameter combination for each algorithm. To choose the best hyper-parameter combination we use stratified 5-fold cross-validation. A  $k$ -fold cross-validation means that the development set is further split into  $k$ -folds. Each combination of  $(k - 1)$  folds is used for training and the remaining fold serves for testing, for a total of  $k$  train/test splits. The use of a *stratified* 5-fold cross-validation means that each fold has approximately the same class distributions as the original dataset.

Once the optimum combination of hyper-parameters is found, it is used to train a classifier on the 75% development set, and is evaluated on the 25% evaluation set. This final hold-out evaluation set is necessary to accurately estimate real-world performance because the cross-validation can over-fit for the particular split. The performance is measured by computing a skill score for each of the 100 iterations, see Section 5. This allows us to quantify an average performance, but also to evaluate the variance in performance results across different runs. The analysis code can be accessed online<sup>3</sup>.

## 5. Results

To evaluate the performance of the four classifiers we computed for each of the 100 runs the ‘confusion matrix’. A confusion matrix, see Table 1, contains the elements TP (true positive, coronal hole predicted and observed), FP (false positive, coronal hole predicted and filament channel observed), FN (false negative, filament channel predicted and coronal hole observed) and TN (true negative, filament channel predicted and filament channel observed).

There exists a variety of skill scores ([Woodcock, 1976](#)) built by combination of the confusion matrix elements. One of the most frequently used is the Hanssen & Kuipers discriminant also known as true skill statistics (TSS) ([Hanssen and Kuipers, 1965](#); [Bloomfield et al., 2012](#)). The TSS is

---

<sup>3</sup> [https://github.com/rubendv/ch\\_filament\\_classification](https://github.com/rubendv/ch_filament_classification)

Predicted	Observed: Coronal Hole (CH)	Filament Channel (FC)
CH	True Positive (TP)	False Positive (FP)
FC	False Negative (FN)	True Negative (TN)

**Table 1.** Coronal hole and filament channel classification contingency table (confusion matrix).

defined as the proportion of correctly predicted coronal holes among all coronal holes (TPR) minus the proportion of filaments that were classified as coronal holes among all filaments (FPR):<sup>4</sup>

$$\text{TSS} = \text{TPR} - \text{FPR} = \frac{\text{TP}}{\text{TP} + \text{FN}} - \frac{\text{FP}}{\text{FP} + \text{TN}}. \quad (14)$$

The TSS is defined in the range  $[-1, 1]$ . A TSS of 0 indicates that the algorithm cannot distinguish between coronal holes and filament channels. A perfect classifier would have the value 1 or  $-1$  (inverse classification), respectively. In Bloomfield et al. (2012) the TSS was proposed to be the standard skill score for comparing the performances of flare forecasts with differing flare/no-flare sample ratios and is also appropriate for this study. When applying the developed algorithms in the form of an automated coronal hole detection tool we are mainly interested in both, the proportion of correctly predicted coronal holes (TPR) as well as the proportion of falsely predicted coronal holes (FPR). Hence, the combination of TPR and FPR in form of the TSS provides an important and intuitive indicator for the performance of the developed framework. Furthermore, the TSS uses all elements of the confusion matrix and is the only known skill score which is unbiased by the proportion of coronal holes and filament channels in the data sets.

Figure 3 (resp. 4) shows for the intensity based threshold method (resp. for the SPoCA method) the proportion of correctly predicted coronal holes (TPR) (that is, the efficiency or sensitivity) versus the proportion of falsely predicted coronal holes (FPR). The performance for each of the 100 runs is visually represented in those figures by the points (FPR, TPR). A perfect classification would have only points at the position  $(0, 1)$ , a perfect inverse classification points at  $(1, 0)$  and ‘no performance’ is represented by the diagonal line ( $\text{FPR} = \text{TPR}$ ).

Figure 3 shows the performance of the four classifiers using all attributes (from AIA and magnetograms) computed with the intensity-based threshold segmentation maps. All classifiers produce a high TPR, but only the two SVMs achieve at the same time a consistently low FPR, with Linear SVM performing slightly better than SVM. In Figure 4 the results for the SPoCA detection of SVM and Linear SVM are presented. Both classifiers achieve high TPR and low FPR. A comparison of the performance with and without magnetogram information indicates that the inclusion of magnetogram-based attributes in addition to the AIA-based attributes systematically improves both TPR and FPR measures across all four classifiers: Figure 4 compares the density of TPR versus FPR obtained for both SVM classifiers when adding or not the magnetogram information, Table 2

<sup>4</sup> For the reader who is used to the terms ‘recall’ and ‘precision’ we note that recall is equivalent to the TPR, and precision denotes the fraction of correctly predicted coronal holes among all predicted coronal holes. The TSS is given by  $\text{TP}/(\text{TP} + \text{FN}) + \text{TN}/(\text{TN} + \text{FP}) - 1$ , the sum of recalls for coronal holes and filament channels minus a scaling factor of 1.

gives the median TSS and the standard deviation for all tested classifiers, and Figure 5 provides a graphical comparison of the actual TSS values in the form of box plots.

<b>Datasets</b>	<b>True Skill Statistics (TSS)</b>			
	<i>SVM</i>	<i>Linear SVM</i>	<i>Random Forest</i>	<i>Decision Tree</i>
Intensity Threshold (all attributes)	$0.90 \pm 0.07$	$0.94 \pm 0.05$	$0.87 \pm 0.10$	$0.80 \pm 0.15$
SPoCA (all attributes)	$0.89 \pm 0.07$	$0.90 \pm 0.06$	$0.77 \pm 0.11$	$0.68 \pm 0.18$
SPoCA (only attributes from AIA)	$0.82 \pm 0.08$	$0.83 \pm 0.07$	$0.71 \pm 0.11$	$0.63 \pm 0.21$

**Table 2.** Median TSS and standard deviation for all four classifiers and the three different datasets.

For both segmentation techniques best results are achieved with linear SVM showing the highest median TSS and smallest standard deviation. Similar results can be obtained with SVM, although with slightly lower values of the median TSS. In contrast, Decision Tree and Random Forest exhibit significantly lower median TSS and higher standard deviation. For the dataset extracted with the SPoCA algorithm we also considered the case where attributes are obtained from AIA images only. The corresponding performance is, as expected, lower than when magnetogram information is included.

Another comparison of the investigated classifiers is presented by the Receiver Operator Characteristic (ROC) curves. ROC curves are commonly used to compare and evaluate the performance of different classifiers. They characterize how the number of correctly classified coronal holes (TPR) varies with the number of incorrectly classified filament channels (FPR). This gives an illustration of the tradeoff between the completeness of coronal holes and the contamination with filaments for each classifier. Hence, the ROC curves convey the information of which classifier should be applied when either a small, focused sample of coronal holes or a larger sample of coronal holes is requested.

In Figure 6, the ROC curves for SVM and linear SVM calculated from the combined results of each of the 100 iterations are shown. Again, the FPR is plotted on the x-axis and the TPR on the y-axis. The best results are represented by curves close to the upper left corner with a possible large area under the curve (AUC). The AUC is usually used in order to roughly summarize the obtained ROC curves in a single quantity. The best performances, indicated by a high completeness together with a low contamination, are achieved with the Linear SVM followed by the SVM using all computed attributes. The ROC analysis confirms that the exclusion of the magnetogram information negatively affects the performances of both classifiers by decreasing the TPR and increasing the FPR.

## 6. Discussion and Conclusion

The most popular methods for the extraction of coronal hole regions are based on the intensity information in EUV images of the Sun. However, other features, notably filament channels, appear similarly dark as coronal holes. It is a general problem of intensity-value-based techniques to distinguish between those features. We found in our carefully prepared datasets using two different segmentation algorithms (intensity-based thresholding and SPoCA) that about 15% of the

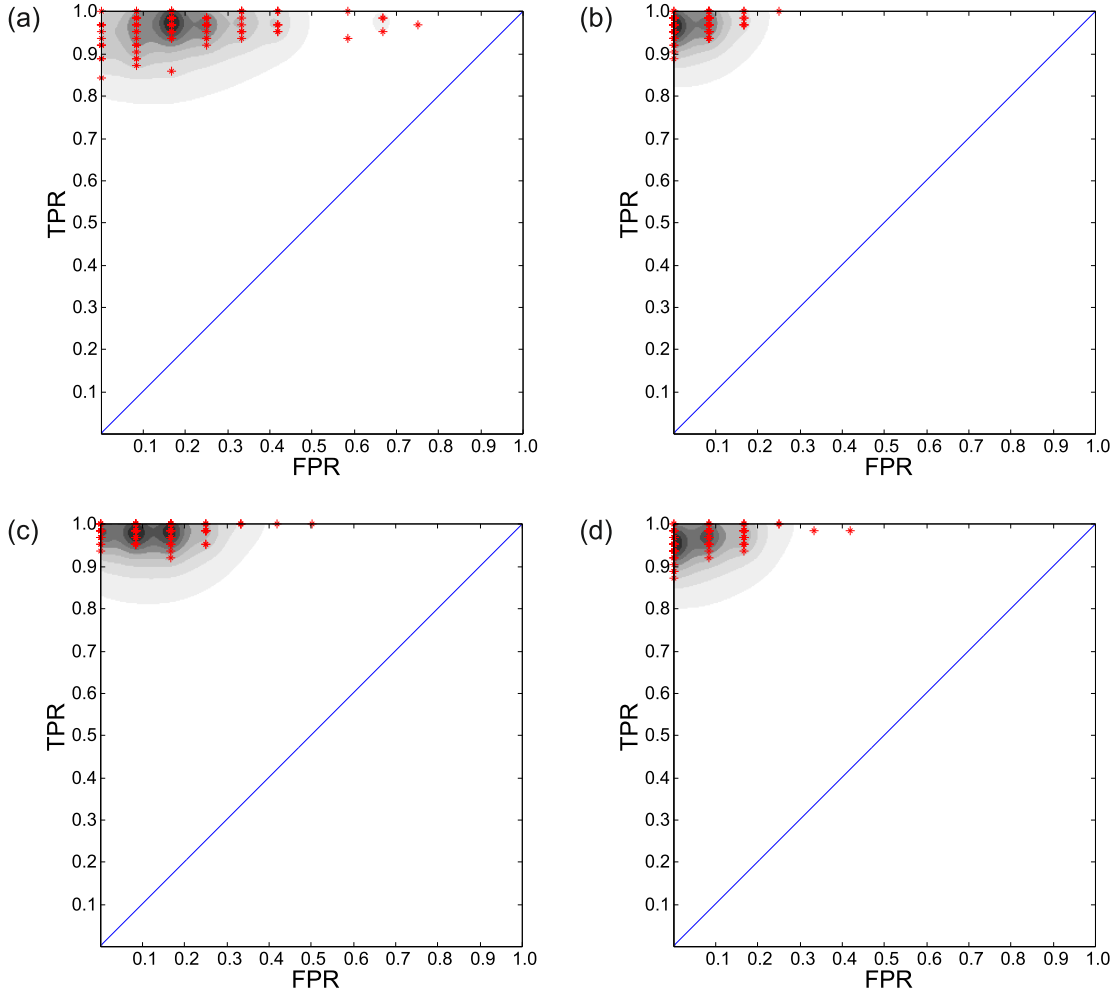


**Fig. 3.** Density plot of correctly predicted coronal holes (TPR) versus erroneously predicted coronal holes (FPR) obtained from intensity-based coronal hole region segmentation using all attributes. The red crosses denote the individual results for the TPR and FPR for each of the 100 iterations, according to the training and evaluation protocol described in Section 4.2. (a) Decision Tree; (b) Linear SVM; (c) Random Forest; (d) SVM.

coronal hole candidates are actually filament channels. We therefore developed new algorithms and techniques to tackle this shortcoming.

We investigated a new approach using a combination of segmentation techniques and machine learning algorithms. The proposed attributes were used as input for supervised classification schemes. Four commonly applied classifiers, including SVM, Linear SVM, Decision Tree and Random Forest were tested for two different segmentation techniques and evaluated based on true skill statistics. The results reveal that all classifiers provide good results in general, with the linear SVM and SVM classifier providing the best performances ( $TSS \approx 0.90$ ). We also found that the two different image segmentation techniques provide very similar results indicating the broad applicability of the presented method. In addition to EUV images we used the magnetic field information

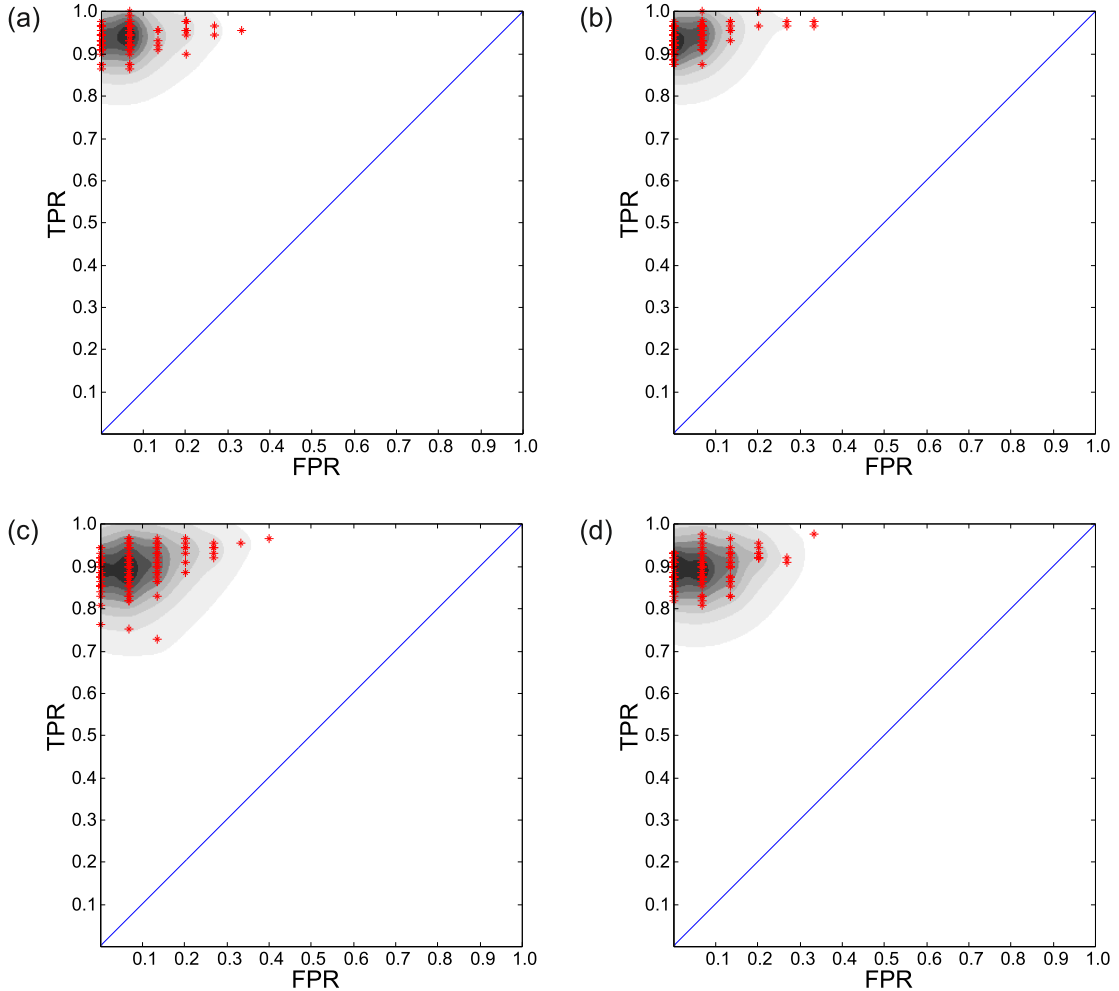


**Fig. 4.** Density plot of correctly predicted coronal holes (TPR) versus erroneously predicted coronal holes (FPR) obtained with SPoCA algorithm. The red crosses denote the individual results for the TPR and FPR for each of the 100 iterations, according to the training and evaluation protocol described in Section 4.2. (a) SVM (all attributes); (b) Linear SVM (all attributes); (c) SVM (AIA attributes only); (d) Linear SVM (AIA attributes only).

from HMI line-of-sight magnetograms. Adding the information and extracted attributes from the magnetic field data improves the performance across all four classifiers for the SPoCA detection (c.f. Table 2).

Besides standard statistical attributes we investigated the benefits from textural features, originally introduced by Haralick et al. (1973), to analyze the texture information of coronal holes and filament channels in high spatial resolution AIA 19.3 nm and line-of-sight magnetograms. For this purpose we adapted the original method introduced by Haralick to open value ranges in order to calculate a set of textural features for intensity and magnetic field configurations. This enabled us to describe the intrinsic spatial arrangement contained within coronal hole and filament channel regions in AIA 19.3 nm and line-of-sight magnetograms with a set of textural features. Textural

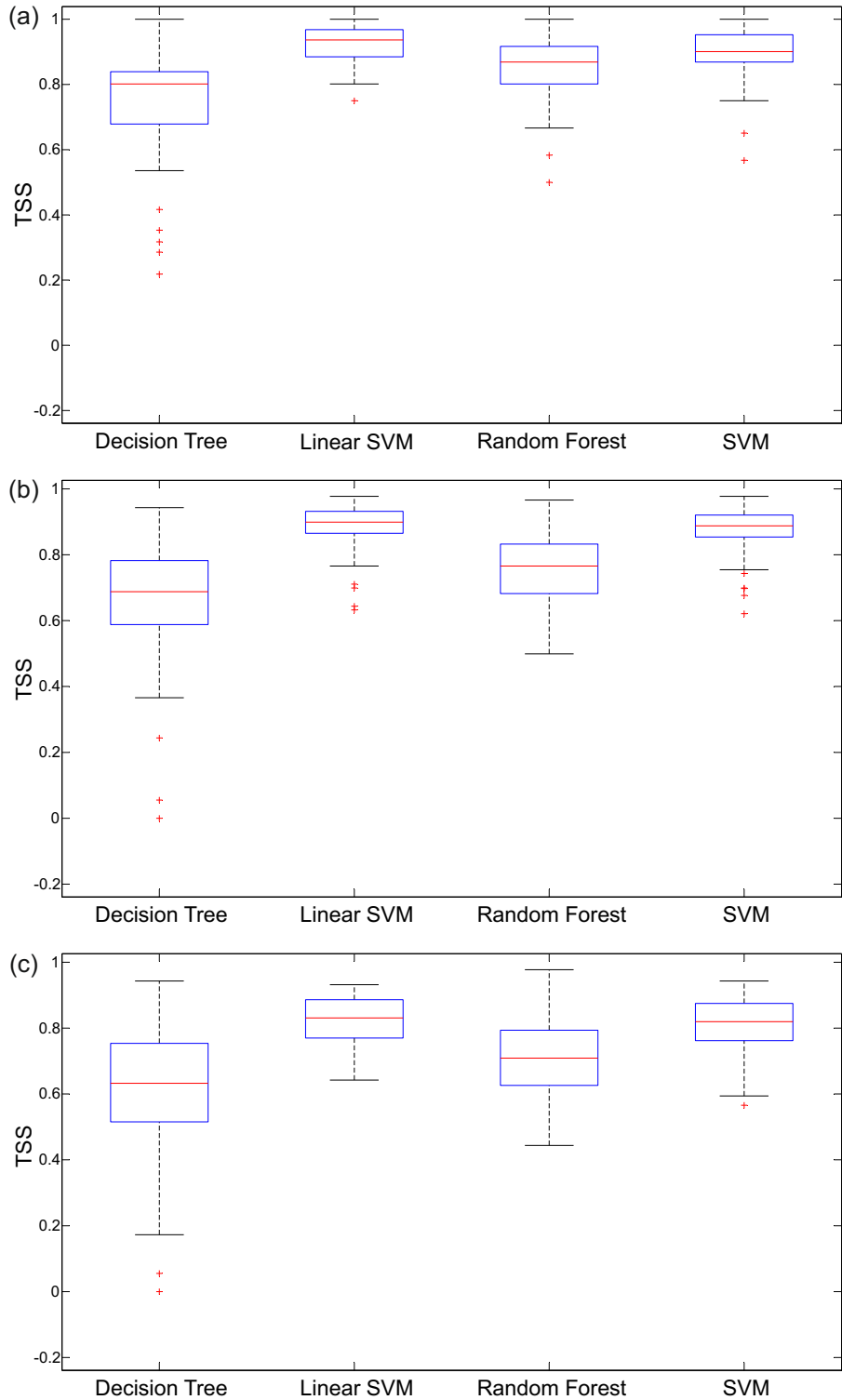


**Fig. 5.** Comparison between the computed true skill statistics (TSS) for different classifiers using different segmentation techniques and sets of attributes. On each box, the central mark is the median (50th percentile), the edges of the box are the 25th and 75th percentiles, the whiskers show the  $\pm 2.7\sigma$  range covering 99.3% of the data and outliers are plotted individually as red crosses. (a) Intensity Threshold (all attributes) (b) SPoCA (all attributes); (c) SPoCA (only attributes from AIA).

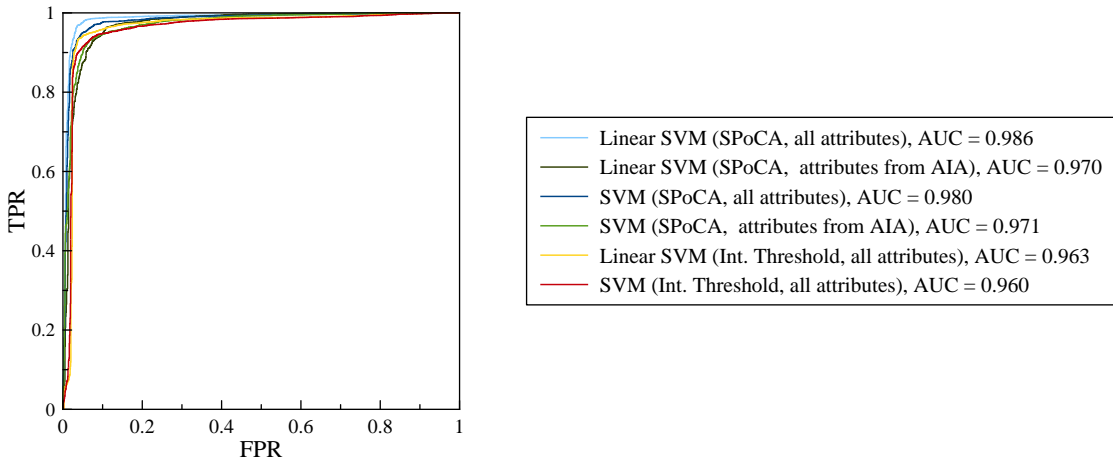


**Fig. 6.** ROC curves for the SVM and Linear SVM classifier together with the calculated area under the curve (AUC).

features provide information about the structural arrangement of pixel values in contrast to first order statistics, which focus on the overall pixel value distribution contained in an image. In this respect we note that for the detailed analysis of textural features one has to take into account the influence of noise. Digital images are discrete representations of objects or scenes, unavoidably, they have limited spatial resolution and they are contaminated with noise (Delouille et al., 2008). Hence, the image quality is a limiting factor for using such kind of methods and low signal to noise ratios may hinder the application of textural information.

The algorithms are not costly with respect to computing-time. The segmentation algorithms as well as the calculation of attributes and classifiers are calculated within a few minutes. This is favorable for real-time application. We therefore aim to implement the described algorithms in currently available forecasting tools for solar wind high speed streams<sup>5</sup>. We also plan on improving the SPoCA-CH module within the SDO EDS pipeline using Linear SVM classification on AIA attributes.

In summary, this study demonstrates how a machine learning approach may help improve upon an unsupervised feature extraction method<sup>6</sup>. The findings suggest that the proposed attributes and classifiers may actually be applicable for a wide range of imaging data. We stress that the inclusion of magnetic field data improved the performance of the coronal hole and filament discrimination in EUV images. All tested classifiers provide good results for the TSS and we therefore expect that the developed detection tool has the potential to reduce coronal hole classification error rate for both segmentation algorithms.

*Acknowledgements.* We gratefully acknowledge the NAWI Graz funding *Förderung von JungforscherInnengruppen 2013–15*. The research leading to these results has received funding from the European Commission’s Seventh Framework Programme (FP7/2007-2013) under the grant agreement no. 284461 [eHEROES]. R. DV. and V.D. acknowledge support from the Belgian Federal Science

<sup>5</sup> e.g., [swe.uni-graz.at/solarwind](http://swe.uni-graz.at/solarwind) run by UNIGRAZ

<sup>6</sup> The machine learning code used for the present analysis is available at [https://github.com/rubendv/ch\\_filament\\_classification](https://github.com/rubendv/ch_filament_classification)

Policy Office through the BRAIN.be and the ESA-PRODEX programs. M. T. acknowledges the Fonds zur Förderung wissenschaftlicher Forschung (FWF): V195-N16. M.A.R. acknowledges support from the association *Dynamics of the Solar System* to finance a one-month stay at the Royal Observatory of Belgium. We thank P. Dupont, N. Sabathiel and T. Rotter for insightful discussions. The editor thanks Shaun Bloomfield and Jake VanderPlas for their assistance in evaluating this paper.

## References

- Ahammer, H., J. M. Kröpfl, C. Hackl, and R. Sedivy. Image Statistics and Data Mining of Anal Intraepithelial Neoplasia. *Pattern Recogn. Lett.*, **29**(16), 2189–2196, 2008. 10.1016/j.patrec.2008.08.008.
- Anscombe, F. J. The transformation of Poisson, binomial and negative-binomial data. *Biometrika*, **35**, 246–254, 1948.
- Barra, V., V. Delouille, and J. F. Hochedez. Segmentation of Extreme Ultraviolet Solar Images using a Multispectral Data Fusion Process. In Fuzzy Systems Conference, 2007. FUZZ-IEEE 2007. IEEE International, 1–6, 2007. 10.1109/FUZZY.2007.4295367.
- Bezdek, J. C. Pattern Recognition with Fuzzy Objective Function Algorithms. Kluwer Academic Publishers, Norwell, MA, USA, 1981.
- Bloomfield, D. S., P. A. Higgins, R. T. J. McAteer, and P. T. Gallagher. Toward Reliable Benchmarking of Solar Flare Forecasting Methods. *ApJ*, **747**, L41, 2012. 10.1088/2041-8205/747/2/L41, [1202.5995](#).
- Breiman, L. Arcing classifier. *Ann. Statist.*, **26**(3), 801–849, 1998. 10.1214/aos/1024691079, URL <http://dx.doi.org/10.1214/aos/1024691079>.
- Breiman, L., J. Friedman, R. Olshen, and C. Stone. Classification and Regression Trees. Chapman & Hall, New York, 1984.
- Chang, C.-C., and C.-J. Lin. LIBSVM: A library for support vector machines. *ACM Transactions on Intelligent Systems and Technology*, **2**, 27:1–27:27, 2011. Software available at <http://www.csie.ntu.edu.tw/~cjlin/libsvm>.
- Cranmer, S. R. Coronal Holes. *Living Reviews in Solar Physics*, **6**, 3, 2009. 10.12942/lrsp-2009-3, [0909.2847](#).
- de Toma, G. Evolution of coronal holes and implications for high-speed solar wind during the minimum between cycles 23 and 24. *Sol. Phys.*, **274**, 195–217, 2011. 10.1007/s11207-010-9677-2.
- Delouille, V., P. Chainais, and J.-F. Hochedez. Spatial and Temporal Noise in Solar EUV Observations. *Sol. Phys.*, **248**, 441–455, 2008. 10.1007/s11207-008-9131-x.
- Fan, R.-E., K.-W. Chang, C.-J. Hsieh, X.-R. Wang, and C.-J. Lin. LIBLINEAR: A library for large linear classification. *Journal of Machine Learning Research*, **9**, 1871–1874, 2008.
- Gosling, J. T., and V. J. Pizzo. Formation and Evolution of Corotating Interaction Regions and their Three Dimensional Structure. *Space Sci. Rev.*, **89**, 21–52, 1999. 10.1023/A:1005291711900.

- Hanssen, A., and W. Kuipers. On the Relationship Between the Frequency of Rain and Various Meteorological Parameters: (with Reference to the Problem Of Objective Forecasting). Koninkl. Nederlands Meterologisch Institut. Mededelingen en Verhandelingen. Staatsdrukkerij- en Uitgeverijbedrijf, 1965.
- Haralick, R. M., K. Shanmugam, and I. Dinstein. Textural Features for Image Classification. *Systems, Man and Cybernetics, IEEE Transactions on*, **SMC-3**(6), 610–621, 1973. 10.1109/tsmc.1973.4309314.
- Hurlburt, N., M. Cheung, C. Schrijver, L. Chang, S. Freeland, et al. Heliophysics Event Knowledgebase for the Solar Dynamics Observatory (SDO) and Beyond. *Sol. Phys.*, **275**, 67–78, 2012. 10.1007/s11207-010-9624-2, [1008.1291](#).
- Japkowics, N., and M. Shah. Evaluating Learning Algorithms: A Classification Perspective. Cambridge University Press, 2014.
- Kirk, M. S., W. D. Pesnell, C. A. Young, and S. A. Hess Weber. Automated detection of EUV polar coronal holes during solar cycle 23. *Sol. Phys.*, **257**, 99–112, 2009. 10.1007/s11207-009-9369-y.
- Krista, L. D., and P. T. Gallagher. Automated coronal hole detection using local intensity thresholding techniques. *Sol. Phys.*, **256**, 87–100, 2009. 10.1007/s11207-009-9357-2.
- Lemen, J. R., A. M. Title, D. J. Akin, P. F. Boerner, C. Chou, et al. The Atmospheric Imaging Assembly (AIA) on the Solar Dynamics Observatory (SDO). *Sol. Phys.*, **275**, 17–40, 2012. 10.1007/s11207-011-9776-8.
- Mackay, D. H., J. T. Karpen, J. L. Ballester, B. Schmieder, and G. Aulanier. Physics of Solar Prominences: II Magnetic Structure and Dynamics. *Space Sci. Rev.*, **151**, 333–399, 2010. 10.1007/s11214-010-9628-0, [1001.1635](#).
- Martens, P. C. H., G. D. R. Attrill, A. R. Davey, A. Engell, S. Farid, et al. Computer Vision for the Solar Dynamics Observatory (SDO). *Sol. Phys.*, **275**, 79–113, 2012. 10.1007/s11207-010-9697-y.
- Müller, D., B. Fleck, G. Dimitoglou, B. W. Caplins, D. E. Amadigwe, J. P. G. Ortiz, B. Wamsler, A. Alexanderian, V. K. Hughitt, and J. Ireland. JHelioviewer: Visualizing Large Sets of Solar Images Using JPEG 2000. *Computing in Science and Engineering*, **11**(5), 38–47, 2009. <http://doi.ieeecomputersociety.org/10.1109/MCSE.2009.142>.
- Munro, R. H., and G. L. Withbroe. Properties of a Coronal “hole” Derived from Extreme-Ultraviolet Observations. *ApJ*, **176**, 511, 1972. 10.1086/151653.
- Pedregosa, F., G. Varoquaux, A. Gramfort, V. Michel, B. Thirion, et al. Scikit-learn: Machine Learning in Python. *Journal of Machine Learning Research*, **12**, 2825–2830, 2011.
- Pötzi, W., A. Veronig, G. Riegler, U. Amerstorfer, T. Pock, M. Temmer, W. Polanec, and D. Baumgartner. Real-time Flare Detection in Ground-Based H $\alpha$  Imaging at Kanzelhöhe Observatory. *Solar Physics*, **290**(3), 951–977, 2015. 10.1007/s11207-014-0640-5, URL <http://dx.doi.org/10.1007/s11207-014-0640-5>.
- Quinlan, J. R. C4.5: Programs for Machine Learning. Morgan Kaufmann Publishers Inc., San Francisco, CA, USA, 1993. ISBN 1-55860-238-0.

Reiss, M. A., M. Temmer, T. Rotter, S. J. Hofmeister, and A. M. Veronig. Identification of coronal holes and filament channels in SDO/AIA 193Å images via geometrical classification methods. *Central European Astrophysical Bulletin*, **38**, 95–104, 2014. [1408.2777](#).

Rotter, T., A. Veronig, M. Temmer, and B. Vršnak. Real-Time Solar Wind Prediction Based on SDO/AIA Coronal Hole Data. *Solar Physics*, **290**(5), 1355–1370, 2015. 10.1007/s11207-015-0680-5, URL <http://dx.doi.org/10.1007/s11207-015-0680-5>.

Rotter, T., A. M. Veronig, M. Temmer, and B. Vršnak. Relation Between Coronal Hole Areas on the Sun and the Solar Wind Parameters at 1 AU. *Sol. Phys.*, **281**, 793–813, 2012. 10.1007/s11207-012-0101-y.

Scherrer, P. H., J. Schou, R. I. Bush, A. G. Kosovichev, R. S. Bogart, et al. The Helioseismic and Magnetic Imager (HMI) Investigation for the Solar Dynamics Observatory (SDO). *Sol. Phys.*, **275**, 207–227, 2012. 10.1007/s11207-011-9834-2.

Tsurutani, B. T., W. D. Gonzalez, A. L. C. Gonzalez, F. L. Guarnieri, N. Gopalswamy, et al. Corotating solar wind streams and recurrent geomagnetic activity: A review. *Journal of Geophysical Research (Space Physics)*, **111**, A07S01, 2006. 10.1029/2005JA011273.

Vapnick, V. Statistical learning theory. Wiley, New York, 1998.

Verbanac, G., B. Vršnak, A. Veronig, and M. Temmer. Equatorial coronal holes, solar wind high-speed streams, and their geoeffectiveness. *A&A*, **526**, A20, 2011. 10.1051/0004-6361/201014617.

Verbeeck, C., V. Delouille, B. Mampaey, and R. De Visscher. The SPoCA-suite: Software for extraction, characterization, and tracking of active regions and coronal holes on EUV images. *A&A*, **561**, A29, 2014. 10.1051/0004-6361/201321243.

Vršnak, B., M. Temmer, and A. M. Veronig. Coronal Holes and Solar Wind High-Speed Streams: I. Forecasting the Solar Wind Parameters. *Sol. Phys.*, **240**, 315–330, 2007. 10.1007/s11207-007-0285-8.

Weyn, B., W. Tjalam, G. V. de Wouwer, A. V. Daele, P. Scheunders, W. Jacob, E. V. Marck, and D. V. Dyck. Validation of nuclear texture density, morphometry and tissue syntactic structure analysis as prognosticators of cervical carcinoma. *Analytical and Quantitative Cytology and Histology*, **22**(5), 373–382, 2000.

Woodcock, F. The Evaluation of Yes/No Forecasts for Scientific and Administrative Purposes. *Monthly Weather Review*, **104**, 1209, 1976. 10.1175/1520-0493(1976)104<1209:TEOYFF>2.0.CO;2.

## Appendix A: Textural Features

### A.1. Notation

We suggest to use a set of textural features which can be calculated from the co-occurrence matrix. The following equations define these features.

$C(i, j)$	$(i, j)$ -th entry in the normalized co-occurrence matrix.
$p_x(i)$	$i$ -th entry is obtained by summing the rows of $C(i, j)$ .
$p_y(j)$	$j$ -th entry is obtained by summing the columns of $C(i, j)$ .
$p_{x-y}(k)$	$k$ -th entry of $p_{x-y}(k)$ corresponding to the sum over all entries of $C(i, j)$ with absolute pixel value difference of $i$ and $j$ equal to $k$ .
$p_{x+y}(k)$	$k$ -th entry of $p_{x+y}(k)$ corresponding to the sum over all entries of $C(i, j)$ where the addition of $i$ and $j$ is equal to $k$ .
$\mu_x, \mu_y$	means of $p_x$ and $p_y$ .
$\sigma_x, \sigma_y$	standard deviations of $p_x$ and $p_y$ .
$N_g$	Number of distinct pixel values.
$\sum_i, \sum_j$	Convention indicating $\sum_{i=1}^{N_g}, \sum_{j=1}^{N_g}$ .
HX, HY	Entropies of $p_x$ and $p_y$

$$p_x(i) = \sum_j C(i, j), \quad p_y(j) = \sum_i C(i, j), \quad (\text{A.1})$$

$$p_{x+y}(k) = \sum_i \sum_j C(i, j), \quad i + j = k, \quad k = 2, 3, \dots, 2N_g, \quad (\text{A.2})$$

$$p_{x-y}(k) = \sum_i \sum_j C(i, j), \quad |i - j| = k, \quad k = 0, 1, \dots, N_g - 1, \quad (\text{A.3})$$

$$\text{HX} = - \sum_i p_x(i) \log(p_x(i)), \quad \text{HY} = - \sum_i p_y(i) \log(p_y(i)) \quad (\text{A.4})$$

$$\text{HXY1} = - \sum_i \sum_j C(i, j) \log(p_x(i)p_y(j)), \quad (\text{A.5})$$

$$\text{HXY2} = - \sum_i \sum_j p_x(i) p_y(j) \log(p_x(i)p_y(j)), \quad (\text{A.6})$$

### A.2. Textural Features

Based on this notation, the following textural features can be calculated:

Energy:

$$H_1 = \sum_i \sum_j C(i, j)^2, \quad (\text{A.7})$$

Contrast:

$$H_2 = \sum_i \sum_j (i - j)^2 C(i, j), \quad (\text{A.8})$$

Correlation:

$$H_3 = \sum_i \sum_j \frac{(i - \mu_x)(j - \mu_y)}{\sigma_x \sigma_y}, \quad (\text{A.9})$$

Sum of Squares - Variance:

$$H_4 = \sum_i \sum_j (i - \mu)^2 C(i, j), \quad (\text{A.10})$$

Homogeneity:

$$H_5 = \sum_i \sum_j \frac{C(i, j)}{1 + (i - j)^2}, \quad (\text{A.11})$$

Sum Average:

$$H_6 = \sum_{i=2}^{2N_g} i p_{x+y}(i), \quad (\text{A.12})$$

Sum Variance:

$$H_7 = \sum_{i=2}^{2N_g} (i - H_8)^2 p_{x+y}(i), \quad (\text{A.13})$$

Sum Entropy:

$$H_8 = - \sum_{i=2}^{2N_g} p_{x+y}(i) \log(p_{x+y}(i)), \quad (\text{A.14})$$

Entropy:

$$H_9 = - \sum_i \sum_j C(i, j) \log(C(i, j)), \quad (\text{A.15})$$

Difference Variance:

$$H_{10} = \text{var}(p_{x-y}), \quad (\text{A.16})$$

Difference Entropy:

$$H_{11} = - \sum_{i=0}^{N_g-1} p_{x-y}(i) \log(p_{x-y}(i)), \quad (\text{A.17})$$

Information Measures of Correlation (I):

$$\frac{H_9 - \text{HXY1}}{\max(\text{HX}, \text{HY})} \quad (\text{A.18})$$

Information Measures of Correlation (II):

$$H_{13} = \sqrt{1 - \exp(-2(\text{HXY2} - H_9))}. \quad (\text{A.19})$$